High-Performance Chemical Sensing Using Schottky-Contacted Chemical Vapor Deposition Grown Monolayer MoS_2 Transistors

Bilu Liu,[†] Liang Chen,[†] Gang Liu, Ahmad N. Abbas, Mohammad Fathi, and Chongwu Zhou*

Department of Electrical Engineering, University of Southern California, Los Angeles, California 90089, United States. [†]These authors contributed equally to this work.

ABSTRACT Trace chemical detection is important for a wide range of practical applications. Recently emerged two-dimensional (2D) crystals offer unique advantages as potential sensing materials with high sensitivity, owing to their very high surface-to-bulk atom ratios and semiconducting properties. Here, we report the first use of Schottky-contacted chemical vapor deposition grown monolayer MoS_2 as high-performance room temperature chemical sensors. The Schottky-contacted MoS_2 transistors show current changes by 2−3 orders of magnitude upon exposure to very low concentrations of NO_2 and NH_3. Specifically, the MoS_2 sensors show clear detection of NO_2 and NH_3 down to 20 ppb and 1 ppm, respectively. We attribute the observed high sensitivity to both well-known charger transfer mechanism and, more importantly, the Schottky barrier modulation upon analyte molecule adsorption, the latter of which is made possible by the Schottky contacts in the transistors and is not reported previously for MoS_2 sensors. This study shows the potential of 2D semiconductors as high-performance sensors and also benefits the fundamental studies of interfacial phenomena and interactions between chemical species and monolayer 2D semiconductors.

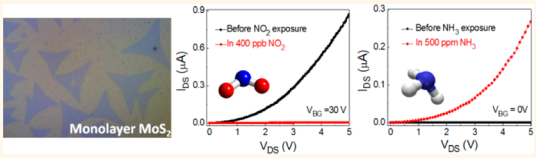

KEYWORDS: MoS_2 · 2D materials · chemical vapor deposition · chemical sensing · charge transfer · Schottky barrier

Environmental pollutant monitoring and trace chemical detection are important issues for both military and civilian purposes. Among air pollutants, toxic gaseous species such as nitrogen oxide (NO_2) and ammonia (NH_3) are two of the most common ones[1] which can be generated from emissions of vehicles, power plants, and off-road equipment. NO_2 in ambient conditions contributes to the formation of ground-level ozone and acid rain and leads to fine particle pollution. Exposure to NO_2 may cause chronic bronchitis, emphysema, and respiratory irritation. On the other hand, exposure to NH_3 may lead to temporary blindness, pulmonary edema, and respiratory irritation.[2] Due to these environmental and health concerns, taking NO_2 as an example, the U.S. Department of Environmental Protection Agency (EPA) has set a primary standard of 53 ppb (parts per billion) for NO_2,[2] NO_2 above which may cause possible health problems especially for those sensitive populations including children, elderly, and people with asthma. Therefore, it is crucially important to develop high-performance sensors that are capable of detecting such toxic gases quickly and reliably even at very low concentrations, for example, ppb level.

Nanomaterials hold promising potential toward these requirements due to their large surface-to-volume ratio and intrinsic small dimension, which enable the fabrication of ultrasensitive chemical and biological sensors with minimized dimensions and consequently high packing densities.[3−9] In this connection, various nanomaterials including carbon nanotubes,[3−5,10] silicon nanowires,[6−9] and metal oxide nanowires and nanobelts[11−15] have been demonstrated to show high sensitivity to a large variety of gas molecules and chemical and biological species.

Two-dimensional materials (2D materials) such as graphene, in the monolayer state, offer the highest surface-to-volume ratio and can provide ultimate sensitivity down to the single-molecule level.[16,17] Abundant effort has been made in the fabrication of graphene-based chemical and biosensors. Previous studies have also shown that proper gating of the sensors may offer them with

* Address correspondence to chongwuz@usc.edu.

Received for review March 18, 2014 and accepted April 16, 2014.

Published online April 21, 2014
10.1021/nn5015215

optimal sensitivity.[6] Noticeably, layered transition metal dichalcogenides (TMDCs), such as MoS_2, share similar 2D structures with graphene, which render them very high surface areas. Moreover, recent theoretical and experimental studies have confirmed that monolayer MoS_2 is a direct band gap semiconductor with impressive device performance.[18−20] This offers gate-tunable conductance for MoS_2 field-effect transistors (FETs).[18,20−23] In addition, the contact property between MoS_2 and metal electrodes sensitively depends on not only the types and work functions of contact materials[24−28] but also the annealing recipes and contact area of metal/MoS_2,[18,26,29,30] offering a way to tune the nature of contacts in MoS_2 devices. These features render MoS_2 a potential chemical sensing material. Mechanically exfoliated monolayer to few-layer MoS_2 have been demonstrated as promising sensing materials for chemical and biological species including NO, NO_2, NH_3, nerve gases, proteins, *etc.*[31−35] For example, Li *et al.* presented a detection limit of ~800 ppb of NO,[32] and Late *et al.* showed a detection limit of a few hundred parts per million (ppm) for both NH_3 and NO_2 using mechanically exfoliated few-layer MoS_2 FETs.[33] Interestingly, in those studies,[32,33] the authors found that monolayer MoS_2 devices were not stable for sensing applications. Very recently, Perkins *et al.* have reported highly sensitive detection of nerves gases using mechanically exfoliated monolayer MoS_2-based FETs.[34] It is therefore interesting to study whether monolayer MoS_2 can be a good sensing material or not since the monolayer is the ultimate form of these 2D materials. On the other hand, taking NO_2 as an example, the reported detection limit of the current MoS_2 sensors (*e.g.*, a few ppm to a few hundred ppm) is still moderate and higher than the primary standard set by the EPA (*i.e.*, 53 ppb). Clearly, more effort should be devoted to MoS_2-based sensing devices to understand their working principle as well as to develop devices with higher sensitivity to fulfill the application needs. Another consideration is that mechanical exfoliation, which is used to prepare MoS_2 materials for sensing in most of the recent studies, is not suitable for large-scale fabrication of sensors, and more scalable methods should be developed. Since MoS_2 is a layered material with most of its atoms being directly exposed to ambient conditions, it is also of fundamental importance to study the interaction and chemical reactions between gaseous species and the surface of the monolayer 2D semiconducting materials, about which little is currently known.

In this article, we report chemical vapor deposition (CVD) growth of monolayer MoS_2 in a three-zone tube furnace. We demonstrate the first use of CVD-grown monolayer MoS_2 transistors with Schottky contacts for the ultrasensitive detection of NO_2 down to a few ppb level and NH_3 down to 1 ppm and potentially even lower concentration. Considering their atomic thickness and good mechanical robustness,[36] this work shows that the 2D MoS_2 monolayer stands as a competitive candidate for high-performance room temperature gas sensors.

RESULTS AND DISCUSSION

We followed recent work for the CVD growth of monolayer MoS_2[37−49] with some modifications, and details of monolayer MoS_2 growth can be found in the Experimental Section. Here, a three-zone CVD furnace (Figure 1a) was used to grow MoS_2 monolayers, and the temperature of each zone can be controlled separately. Sulfur powder was used as solid sulfur source and was placed at the first zone. MoO_3 powder was used as the Mo source which was placed at the second or the third zone. The growth substrates, SiO_2/Si, were placed facing downward on top of the quartz boat hosting the MoO_3 powders (Figure 1a). The furnace was ramped up to the growth temperature of 625 °C rapidly in 7 min, and MoS_2 growth lasted for 5−15 min, which resulted in either isolated triangular monolayers or quasi-continuous films (Supporting Information Figure S1). More details regarding MoS_2 growth are given in the Experimental Section. Figure 1b shows a typical optical microscopic image of the as-grown triangle-shaped materials, which are light blue under the optical microscope. The lateral dimensions of these triangles are found to be 5−30 μm. In addition to the large triangles, detailed atomic force microscopy (AFM) characterization also shows the existence of some small triangles, with lateral size of ~1 μm or smaller, located around the large sheets and can be barely seen under an optical microscope. Interestingly, bright dots or triangles are frequently found at the center of the large triangles (Figure 1c and Figure S1), which we speculate acted as "seeds" for initial nucleation of MoS_2 monolayers.[41] The effectiveness of seeds in promoting the CVD growth of monolayer MoS_2 has also been reported recently by Ling *et al.*[50] Our Raman characterization shows that these dots are multilayer MoS_2 in our samples (Figure S1e,f). The degree of surface coverage can be tuned by the growth time, ranging from isolated individual domains (Figures 1b and S1a,b) to quasi-continuous films (Figure S1c,d). The crystalline nature of the MoS_2 was also confirmed by high-resolution transmission electron microscopy (TEM) characterization with a spacing of ~0.27 nm for the (100) crystal planes (Figure 1d).

Raman spectroscopic and photoluminesence (PL) spectroscopic studies were conducted to evaluate the number of layers and the optical quality of the grown materials. Shown in Figure 1e are representative Raman spectra of the large triangles, where the distance between the in-plane E_{2g}^1 mode and out-of-plane A_{1g} mode is 18−21 cm^{-1}, indicating the formation of predominately monolayer MoS_2, consistent with early reports.[37−39,41−43] One interesting property of

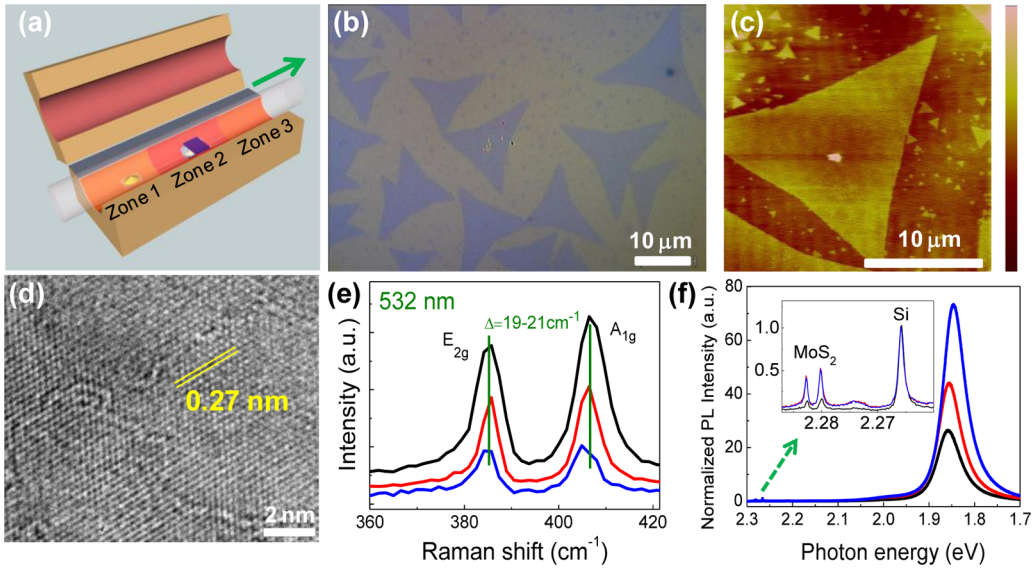

Figure 1. Growth and characterization of monolayer MoS_2 using a three-zone CVD furnace. (a) Schematic of the three-zone CVD furnace used for MoS_2 monolayer growth. Sulfur was put in zone 1, and the MoO_3 precursor and the growth substrates were put in zone 2 or zone 3. The temperatures of the three zones can be controlled separately. (b) Optical microscopy image of the as-grown MoS_2 monolayers on 300 nm SiO_2/Si substrates. (c) AFM image of the as-grown MoS_2. The height scale bar is 12 nm. (d) High-resolution TEM image of a MoS_2 monolayer. (e,f) Raman and normalized PL spectra of monolayer MoS_2 from different samples. Inset of (f) shows the normalized Raman peak of the silicon substrates (2.266 eV) and two Raman peaks from MoS_2 (2.283 and 2.280 eV). The Raman and PL measurements were performed using a 532 nm laser.

monolayer MoS_2 is that it is a direct band gap semiconductor with strong PL, showing sharp contrast with its bulk counterpart, which is an indirect band gap semiconductor with negligible quantum yield.[51,52] Our PL studies show that the samples show a dominated single PL peak at ~1.85 to 1.86 eV (Figure 1f), which has an exceptionally high intensity (for example, >70 times higher than the Raman peaks from the SiO_2/Si substrate located at ~2.266 eV; see the blue spectrum in Figure 1f). We have measured tens of different samples and found that they possess very similar Raman and PL characteristics, indicating the high uniformity of the products.

Layered materials like graphene and MoS_2 possess the highest possible surface-to-volume ratio when they are in monolayer states, and it is expected that these materials may offer ultrahigh sensitive detection of various chemical species. The semiconducting nature of MoS_2 may render efficient gate modulation of the conductance in FETs, which adds another freedom to manipulate the properties of devices.[6,15] Such studies may also benefit the fundamental understanding of the gas−solid interactions and interfacial phenomena. We have fabricated bottom-gated FETs directly on the SiO_2/Si substrates where MoS_2 were grown. The devices were fabricated using e-beam lithography, and 5 nm Ti/50 nm Au was deposited as source and drain electrodes (see Experimental Section). Figure 2a shows a schematic diagram of the device configuration in this study. An optical image of two fabricated devices is shown in Figure 2b with channel length of ~1 μm and channel width being determined by the size of the MoS_2 sheets and the positions of the electrodes (dotted white lines indicate the position of MoS_2 in one device). Typical output ($I_{DS}-V_{DS}$) and transfer characteristics ($I_{DS}-V_{BG}$) of a MoS_2 FET are shown in Figure 2c,d. Figure 2d shows n-type transistor behavior for MoS_2 FETs, consistent with an n-type semiconducting nature of MoS_2 and recent electrical transport measurements on mechanically exfoliated or CVD-grown MoS_2.[21,22,41,42] The effective mobility and on/off current ratios of our CVD-grown MoS_2 in a bottom-gate FET configuration range from 0.2 to 3 cm^2/Vs and 10^4 to 10^6, respectively, which are comparable with the mechanically exfoliated or CVD-grown monolayer MoS_2 under similar device configuration.[21,37,38,41,42,53]

We notice that there is considerable level of Schottky barrier (SB) existing in our devices with Ti/Au electrodes, as evidenced by the output characteristics ($I_{DS}-V_{DS}$) of MoS_2 devices from negative to positive V_{DS} range, which show the rectifying characteristic of as-fabricated MoS_2 devices (Figure 2c and Figure 3a,b). The shape of $I_{DS}-V_{DS}$ originates from MoS_2 devices with Schottky contacts at both source and drain sides, consistent with a very recent study using Co contact.[54] All of the as-fabricated MoS_2 devices (without annealing) show similar Schottky contact behavior. Such devices were used for sensing studies reported later.

We have performed systematical low-temperature measurements to quantitatively determine the height of SB (Figure 3). We used the 2D thermionic emission equation to describe the electrical transport behavior of Schottky-contacted MoS_2 devices following Kawakami's

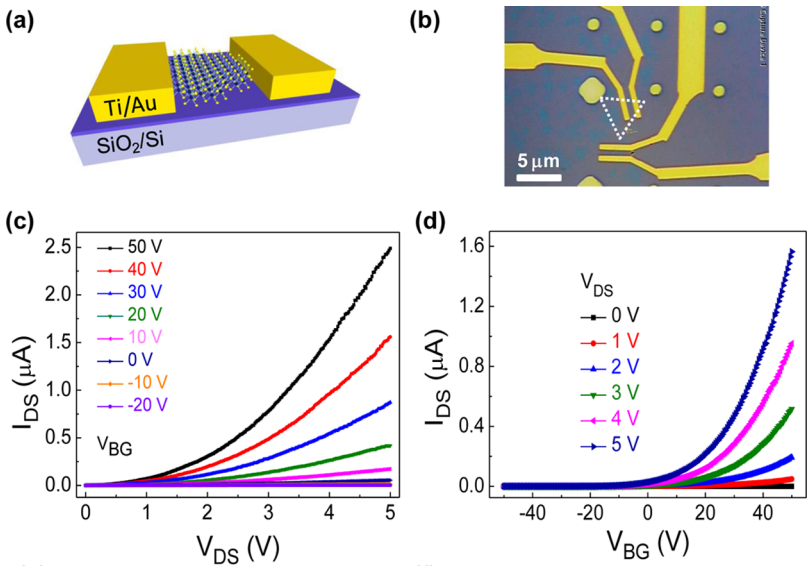

Figure 2. Device characteristics of MoS_2 FETs. (a) Schematic of the back-gate MoS_2 FET in this study. (b) Optical image of two devices. (c,d) Typical output ($I_{DS}-V_{DS}$) and transfer characteristics ($I_{DS}-V_{BG}$) of the MoS_2 FETs.

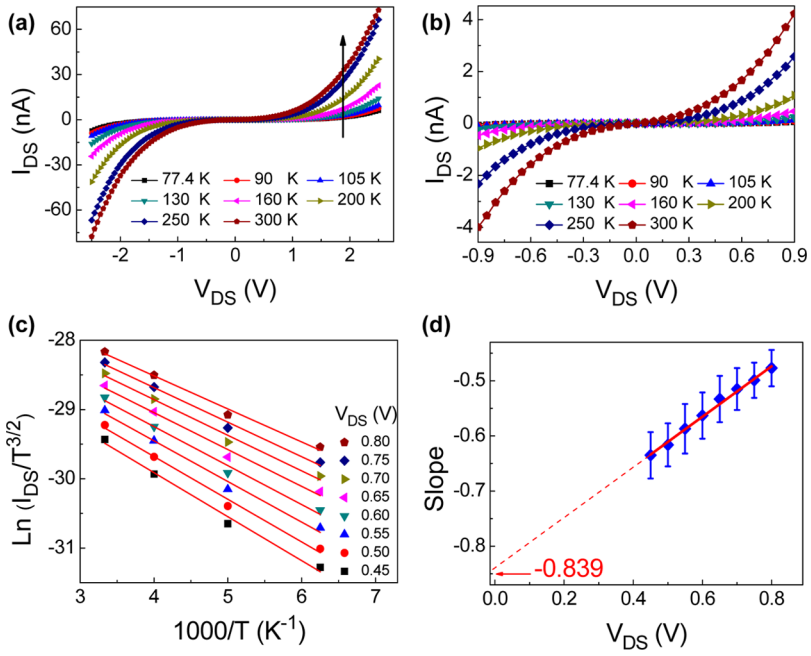

Figure 3. Temperature-dependent transport measurements of MoS_2 FETs. (a) $I_{DS}-V_{DS}$ characteristics of the devices at different temperatures from 77.4 to 300 K. The V_{DS} spans from negative to the positive range and V_{BG} = 40 V. (b) Zoom-in plot of the $I_{DS}-V_{DS}$ characteristics at low V_{DS} regime. (c) Linear fit of the Arrehenius plot, $\ln(I_{DS}/T^{3/2})$ *versus* 1000/T (at temperatures of 160, 200, 250, and 300 K), and a slope can be obtained at each V_{DS}. (d) Slopes extracted from (c) as a function of V_{DS}. Linear fitting of the slope *versus* V_{DS} gives a *y*-intercept of −0.839.

recent report:[54]

$$I_{DS} = AA^*_{2D}T^{3/2}\exp\left[-\frac{q}{k_BT}\left(\Phi_B - \frac{V_{DS}}{n}\right)\right] \quad (1)$$

Here, A is the contact area of the MoS_2−electrode junction, A^*_{2D} is the two-dimensional equivalent Richardson constant, T is the absolute temperature, q is the magnitude of the electron charge, k_B is the Boltzmann constant, Φ_B is the height of the Schottky barrier, and n is the ideality factor. In addition, a reduced power law of $T^{3/2}$ instead of T^2 is used for the two-dimensional transport system.

Figure 3c plots the linear fit of the Arrehenius plot, $\ln(I_{DS}/T^{3/2})$ *versus* 1000/T (at temperatures of 160, 200, 250, and 300 K), and a slope can be obtained at each V_{DS}. Figure 3d plots the slopes extracted from Figure 3c as a function of V_{DS}. Linear fitting of the slope *versus* V_{DS} gives a *y*-intercept of −0.839. Based on eq 1, the height

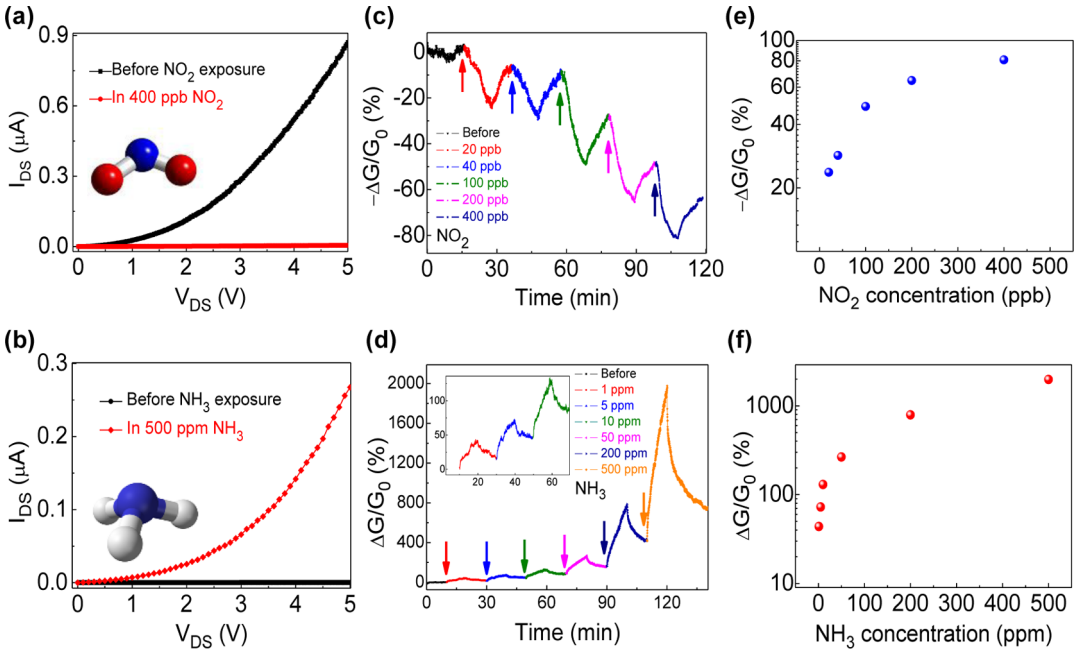

Figure 4. Sensing performance of MoS_2 FETs to NO_2 and NH_3. (a,b) Conductance change of MoS_2 FETs upon exposure to 400 ppb of NO_2 (a) and 500 ppm of NH_3 (b). The devices were initially turned on at V_{BG} = 30 V in (a) and turned off at V_{BG} = 0 V in (b). A conductance decrease by a factor of 174 was achieved in (a) and increase by a factor of 1218 was achieved in (b). (c,d) Real time conductance change of MoS_2 FETs with time after exposure to NO_2 (c) and NH_3 (d) under different concentrations. The arrows in (c) and (d) indicate the time when the corresponding concentrations of gas were introduced. Inset in (d) is a zoom-in plot of the sensor response to low concentrations of NH_3 of 1, 5, and 10 ppm. (e,f) Conductance change *versus* NO_2 concentration (e) and NH_3 concentration (f) based on MoS_2 FET sensors.

of the SB can be deduced as follows:

$$y_{\text{intercept}} = -\frac{q}{1000k_B}\Phi_B \qquad (2)$$

Therefore, the height of the SB was determined to be 72.4 meV for this device, with a standard error of 6.5 meV. We have measured a few devices, and the SB heights are in the range of 52.6 to 82.0 meV. We note this shows reasonably good agreement with a recent study where a SB height of 50 meV was obtained for Ti-contacted MoS_2 devices.[27]

The high surface area of monolayer MoS_2 renders it very susceptible to variation in ambient conditions. For example, the devices exhibit different on-state current and hysteresis in air and in argon, indicating the effect of environment on the transport properties of the MoS_2 (Figure S2).[55] To study the gas−solid interaction and to get a qualitative picture on the conductance modulation of MoS_2 monolayers by gas exposure, we chose NO_2 and NH_3, the two representative toxic gases with rather different electron affinity, for illustration. Figure 4a plots the $I_{DS}-V_{DS}$ of a MoS_2 FET upon exposure to 400 ppb of NO_2. The device was gated at V_{BG} = 30 V and was highly conductive before NO_2 exposure. A conductance decrease by a factor of 174 was achieved under such a low concentration of NO_2, indicating the very high sensitivity of our MoS_2 sensor to NO_2. Furthermore, we monitored the conductance change of the MoS_2 FET with exposure to NH_3. The device was gated at V_{BG}= 0 V and showed little conduction before NH_3 exposure, as shown in Figure 4b. We observed a conductance increase of ~1218 times after exposure to 500 ppm of NH_3. We chose different V_{BG} for NO_2 and NH_3 sensing since the threshold regime of the devices may provide better sensitivity.[6] For example, at V_{BG} = 30 V, the device is in on-state before NO_2 exposure. The introduction of NO_2 may make current change more significant than a device initially in the off-state. The same consideration was taken for NH_3 sensing. Collectively, the above results show the high sensitivity and large modulation of conductance of MoS_2 transistors by exposure to NO_2 and NH_3. Moreover, it also reveals the different interaction processes between MoS_2 and those two gaseous species.

Later, we performed systematic chemical sensing studies of MoS_2 FETs toward NO_2 and NH_3 molecules under different concentrations, as shown in Figure 4c,d. Figure 4c shows the real time conductance changes of a representative MoS_2 FET toward exposure to NO_2 at concentrations of 20, 40, 100, 200, and 400 ppb. Clear response (conductance decrease) was observed for all of these concentrations among multiple devices we tested. The sensor response (S) is defined as follows:

$$S = \frac{G_S - G_0}{G_0} \times 100\% = \frac{\Delta G}{G_0} \times 100\% \qquad (3)$$

Here, G_S and G_0 are the conductance of the MoS_2 FETs under certain gas exposure and at an initial state, respectively. Significantly, it can be seen from Figure 4c that even for 20 ppb of NO_2, a sufficiently large response of >20% was achieved, which is superior

to recent reports using exfoliated few-layer MoS_2 for sensing NO_x under a few ppm to even hundreds of ppm concentrations.[31,33] We point out that this is the record detection limit (20 ppb) for NO_2 using 2D TMDCs so far, and it shows several orders of magnitude improvement compared to recent studies. In addition, the clear detection of a few ppb level of NO_2 shares comparable performance with the best nanowire and nanotube-based NO_2 sensing devices.[5,11] Since the response at 20 ppb of NO_2 is sufficiently large, we think that the detection limit can be further pushed to an even lower value by optimizing the device performance. Figure 4d shows the conductance change (increase) of a MoS_2 FET upon exposure to NH_3 with different concentrations of 1, 5, 10, 50, and 500 ppm. Similar to NO_2, clear conductance modulations were observed for each NH_3 concentration. Once again, we noticed that a sufficiently large sensitivity of >40% was achieved with low concentration (1 ppm) of NH_3 exposure, indicating that detection below ppm level of NH_3 is highly possible. The response time of the sensors, which was defined as the time required to achieve a 90% change of the conductance of the overall range at a specific gas concentration, was found to be between 5 and 9 min. This is a direct reflection of the adsorption rate of the sensors, and a response time of several minutes is comparable to sensors based on metal oxides, conducting polymers, and other nanomaterials like carbon nanotubes,[3,11] as well as recent reports on MoS_2 sensors.[32,33] Figure 4e,f shows the sensor response *versus* the concentrations of NO_2 and NH_3, respectively. The sensors show initially rapid conductance change upon exposure to low concentrations of NO_2 and NH_3, and then quasi-saturation behavior was observed for high gas concentrations.

For both NO_2 and NH_3 sensing, we have fabricated multiple devices and conducted sensing experiments with different MoS_2 sensors and repeated measurements on the same MoS_2 sensor after its recovery. Here we found that the MoS_2 sensors can be fully recovered by putting the devices in air for ~12 h at room temperature. Alternatively, ultraviolet irradiation is found to be very efficient to fully recover the devices within a few seconds (data not shown). Among these series of sensing experiments (more than 15 sensing experiments in total), we found that the detection limits of different devices are close to each other (*e.g.*, ~10−20 ppb for NO_2 and 1 ppm for NH_3). The sensor response under certain gas concentration varies by a factor of 2 among different devices. Under repeated measurements of the same device, the sensitivity remains largely unchanged.

It is important to understand the gas−MoS_2 interaction and sensing mechanism in the process. One important question is whether there are chemical reactions that take place and new compounds formed between analyte and MoS_2 sensors. To probe this, we first collected Raman spectra of MoS_2 on five different sheets. Then, the MoS_2 sensor was put in 400 ppb of NO_2 (or 500 ppm of NH_3) for 10 min (the highest gas concentrations and the same amount of time exposure in the sensing experiments). Lastly, we collected Raman spectra at exactly the same positions as collected before, under assistance of markers and electrodes on the substrates. Figure S3 shows representative Raman spectra of pristine and gas exposed MoS_2 for NO_2 (Figure S3a) and NH_3 (Figure S3b). We do not observe the formation of MoO_3 after NO_2 exposure, which is expected to show several strong Raman peaks at 821, 666, and 284 cm^{-1}, *etc.*, as reported by Kalantar-zadeh *et al.*[56−58] Similarly, we do not see any noticeable changes for MoS_2 after exposure to NH_3 either. These results reveal that there are negligible irreversible chemical reactions taking place between NO_2 (or NH_3) and MoS_2 sensors, which is in agreement with our observation that the sensors are fully recovered after long time air storage.

Later, we studied how the device characteristics change upon exposure of gases and tried to shed some light on the understanding of sensing mechanism of MoS_2 sensors (Figure 5). Figure 5a shows the $I_{DS}-V_{BG}$ curves of a MoS_2 FET in different concentrations of NO_2. For this set of experiments, the devices were exposed to corresponding gas concentrations for 10 min and then the $I_{DS}-V_{BG}$ curves were measured. The $I_{DS}-V_{BG}$ curve taken at the initial state (before 20 ppb NO_2 exposure) was also plotted as a reference. A clear monotonic shift of the curves toward positive gate voltage direction is observed, indicating a continuous increase of the threshold gate voltage (V_{th}), as shown quantitatively in Figure 5c. In contrast, a monotonic shift of the $I_{DS}-V_{BG}$ curves, but in the negative gate voltage direction, was observed for NH_3 sensing, as shown in Figure 5b and quantitatively plotted in Figure 5d.

The MoS_2 FET sensor relies on the conductance (resistance) change of the devices upon gas exposure. The resistance of a MoS_2 FET can be expressed as follows.

$$R = R_{channel} + R_{contact} \quad (4)$$

Here, R, $R_{channel}$, and $R_{contact}$ are the total device resistance, the channel resistance from MoS_2, and the contact resistance at metal electrode/MoS_2 junctions, respectively. The channel resistance $R_{channel}$ is inversely proportional to the carrier concentration in MoS_2, while the contact resistance, $R_{contact}$, relates to both electron concentration and the height of the SB and can be expressed as follows:[59]

$$R_{channel} \propto \frac{1}{n} \quad (5)$$

$$R_{contact} \propto \frac{1}{n} e^{(\varphi_{SB}/kT)} \quad (6)$$

where n is the electron concentration in MoS_2, φ_{SB} is the height of SB formed at the MoS_2−electrode junctions, k is

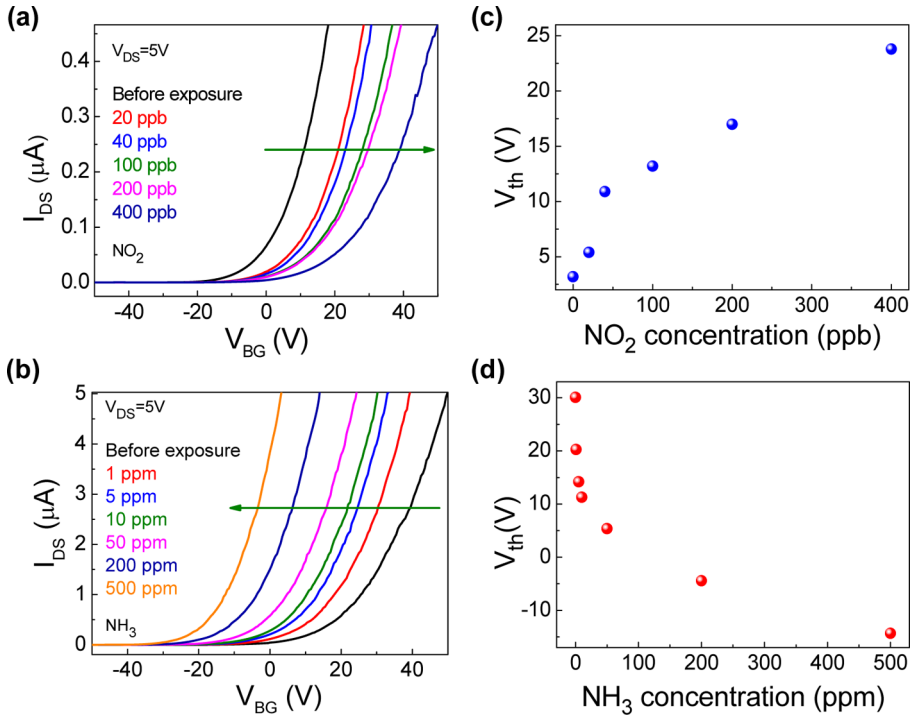

Figure 5. MoS_2 sensing mechanism study. (a,b) Transfer characteristics (I_{DS}–V_{BG}) of MoS_2 FETs upon exposure to NO_2 (a) and NH_3 (b) with different concentrations. (c,d) Threshold voltage (V_{th}) *versus* gas concentrations for NO_2 (c) and NH_3 (d).

the Boltzmann constant, and T is the absolute temperature. Obviously, a change of either electron concentration or SB height can lead to a change in the total resistance (conductance) of the MoS_2 FET and consequently can be reflected in the sensing experiments in Figure 4.

Charge transfer between gaseous species and nanomaterials serves as an important work principle for sensing devices based on nanomaterials. NO_2 is a well-known strong oxidizer due to an unpaired electron from nitrogen atom, which tends to withdraw electrons from sensing materials like MoS_2 studied here. This leads to a decreased electron concentration in the conduction band of the MoS_2, and thus more positive gate voltage is required to turn on the transistor, indicating a positive shift of the V_{th} upon exposure to NO_2 (Figure 5c). NH_3, on the other hand, having a lone electron pair tends to donate electrons to the conduction band of MoS_2, and this would lead to an increased electron concentration in MoS_2, and thus a low gate voltage is required to operate the transistor (Figure 5d). Such a charge transfer mechanism was also used recently to understand the sensing behavior of MoS_2 toward NH_3, NO, and nerve gas by other researchers and showed good agreement with our experimental results.[31,33,34,60] In our experiments, we observed that the detection limit for NO_2 is around 2 orders of magnitude lower than that of NH_3 (*e.g.*, 20 ppb *versus* 1 ppm), which is a common phenomenon observed in many other nanomaterial-based sensors including carbon nanotubes and nanowires.[61] Density functional theory calculations show that NO_2 has much stronger interaction with carbon nanotubes than NH_3 does, which may be responsible for the detection of much lower concentration of NO_2 than NH_3. A very recent calculation on the gas–MoS_2 interaction also shows that NO_2 has a much larger charge transfer ability (10 times larger) than NH_3 with bilayer MoS_2.[33] This, consequently, will lead to a very sensitive detection of NO_2 because a small amount of NO_2 adsorption can cause a substantial change of carrier concentration, which can be reflected through electrical transport measurements.

The charge transfer mechanism suggests that carrier concentration change is the work principle for sensing. A reasonable approximation is that the conductance change of the device should be related to the surface occupancy (θ) of the gas molecules on sensing materials based on a site-binding hypothesis,[61] which assumes that atoms on the surface of the sensing materials can act as binding sites for molecule adsorption. That is

$$\frac{\Delta G}{G_0} \propto \theta \tag{7}$$

The surface coverage of the adsorbed molecules follows a Langmuir isotherm, and this leads to a linear relationship between inverse sensitivity ($1/S$) and the inverse gas concentration ($1/C$), as shown previously for ohmic-contacted In_2O_3 nanowire[11] and graphene nanoribbon[62] chemical sensors. However, the Schottky-contacted MoS_2 sensors do not follow such a linear relationship between $1/S$ and $1/C$ (Figure S4). This suggests that there should be other reasons in addition

to charge transfer that also contribute to the observed sensing behavior.

As there is clear SB in our devices (Figure 3) and according to eq 6, the property of the SB can significantly influence the resistance of the Schottky-contacted devices due to their exponential relationship.[59] Figure 6 shows the schematic of an energy diagram of a Ti/Au electrode and MoS_2 monolayer, where the work functions of Ti (φ_{Ti}) and Au (φ_{Au}) are 4.3 and 5.1 eV, respectively,[59] and the electron affinity (χ) of MoS_2 is ~4.2 eV.[63,64] As we deposited 5 nm Ti/50 nm Au onto MoS_2 to form source/drain electrodes, we may have Ti contacting MoS_2 for most area of the source/drain contacts and Au contacting MoS_2 at the edges of source/drain contacts because the metal evaporation cannot be completely vertical. Therefore, the actual metal contact may be an average effect of both Ti and Au. In addition, we further note that whether there are surface states between metals and 2D materials like MoS_2 has not been well understood, and the presence or absence of surface states may affect the band diagram. Nevertheless, it is still reasonable to assume that, before contact, the Fermi level of Ti/Au lies between the conduction band and valence band of MoS_2 (Figure 6a). After contact, the energy bands bend for MoS_2 and a SB forms with a "nominal" height of

$$\varphi_{SB} = \varphi_{metal} - \chi \quad (8)$$

When MoS_2 devices are exposed to different gases, the conductance change can usually result from a coplay of two factors: charge transfer and SB modulation.[61] The absorption of gas will modify the built-in potential (V_{bi}) and the width of the SB. Specifically, NO_2 absorption can move the Fermi level of MoS_2 toward the valence band. This will increase the width of the SB and decrease the V_{bi} and device current. The opposite is true for NH_3 absorption (Figure 6b). On the other hand, it has been reported that absorbed gas species can change the work function of both metal electrodes and semiconducting materials due to surface dipole layer formation.[61,65−67] In the case of NO_2, it can withdraw electrons and form negatively charged $NO_2^{\delta-}$ species, which may increase the SB height. For example, oxidative species such as oxygen was reported to increase the SB height of a ZnO nanowire transistor.[12] Collectively, both charge transfer and SB modulation are believed to have the same trend to decrease the conductance of MoS_2 devices in the case of NO_2 exposure. On the other hand, NH_3 may hold the opposite trend compared with NO_2. Figure 6b shows the band realignment and energy diagram of the metal−MoS_2 junction after exposure to NO_2 and NH_3, depicting the effects of change of SB height and width (and V_{bi}) upon gas absorption. In addition, we found that some MoS_2 devices show more Ohmic contact after vacuum annealing (see Experimental Section and Figure S5), and the sensing results show that the ohmic-contacted device exhibits little conductance

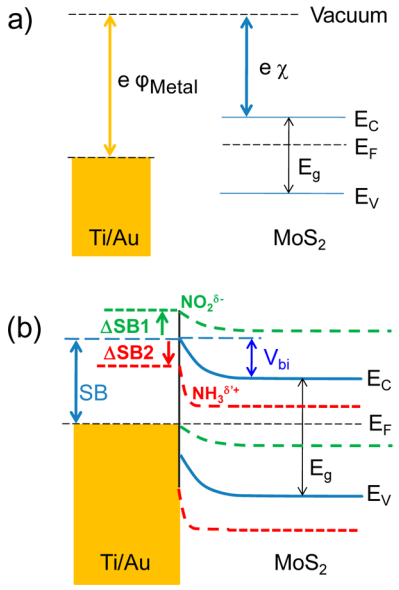

Figure 6. Proposed band alignment diagrams at the MoS_2−metal junctions. (a) Energy diagram of the Ti/Au and MoS_2 before contact. (b) Band realignment and energy diagram of the Ti/Au and MoS_2 after contact and the formation of Schottky barrier. Blue, green, and red lines indicate the energy band of the pristine MoS_2 (solid blue), after exposure to NO_2 (dashed green), and after exposure to NH_3 (dashed red), respectively. NO_2 adsorption increases the SB by ΔSB1 while NH_3 adsorption decreases the SB by ΔSB2. In addition, the built-in voltage (V_{bi}) will decrease (increase) upon NO_2 (NH_3) exposure, resulting in a widening (thinning) of the SB width and a decrease (increase) of the device current.

change (<5%) upon exposure to NO_2 at concentrations up to 400 ppb (Figure S6). This suggests that SB modulation may play a key role in our sensors. Further study is needed to obtain quantitative information about the relative contribution from each mechanism. Interestingly, we also observed that the effective mobility of MoS_2 FETs changed upon NO_2 and NH_3 exposure, and NH_3 exposure increased the effective mobility of MoS_2 (Supporting Information Figures S7 and S8). This finding may serve as an effective strategy to engineer the effective mobility of MoS_2-based electronic devices.

CONCLUSIONS

In conclusion, we have demonstrated room temperature highly sensitive detection of NO_2 and NH_3 using CVD-grown monolayer MoS_2 with Schottky contacts. In particular, 20 ppb of NO_2 and 1 ppm of NH_3 were clearly detected with a conductance change larger than 20 and 40%, respectively, which are much superior to recently reported MoS_2 sensors. Both charge transfer between gaseous species and MoS_2 monolayers and SB modulation at the MoS_2−metal electrode junctions are suggested to be responsible for the observed sensing behavior, while Schottky barrier modulation is believed to be the key factor for the significantly improved sensitivity. The detection

limit can be further pushed to sub-ppb level by optimizing the device performance like the features of the Schottky barrier. Our work demonstrates the potential of these 2D layered semiconductors as strong candidates for gas and chemical sensing applications.

EXPERIMENTAL SECTION

CVD Growth of Monolayer MoS_2. We used a three-zone CVD furnace to grow monolayer MoS_2. In a typical experiment, sulfur (99.95%, 300 mg, Sigma-Aldrich) was put in the first zone with a temperature of ~300 °C during growth. MoO_3 (99.99%, 10 mg, Sigma-Aldrich) was put in the second zone or the third zone with a temperature of 625 °C. The three-zone furnace has a much longer constant temperature zone than the one-zone furnace. Therefore, the use of the three-zone furnace makes it possible to tune the MoO_3 and sulfur distance, while keeping the temperature of MoO_3 unchanged. The growth substrates were SiO_2/Si, which were put on top of the MoO_3 and facing down. The distance between sulfur and MoO_3 was 17−19 cm. The furnace was first pumped down to 0.5 Torr, refilled with high purity Ar until 600 Torr, and repeated once. Then, 50 sccm of Ar was introduced to the system, and the furnace temperature increased to 625 °C rapidly in 7 min. The growth took 2−15 min and was naturally cooled under 50 sccm of Ar after growth.

Characterization. The as-grown MoS_2 was extensively characterized by using optical microscopy, Raman and PL spectroscopy (532 nm laser, Renishaw Raman), and TEM (JEOL 2100F, 200 kV).

Device Fabrication and Measurements. The devices were fabricated using standard e-beam lithography. A poly(methyl methacrylate) (PMMA) layer was first spin-coated onto the SiO_2/Si surface with MoS_2 growth. Then, e-beam lithography was conducted using PMMA as a positive resist. Development, metal deposition, and lift-off processes were conducted successively to fabricate the devices. The electrode materials are made of 5 nm Ti and then 50 nm Au, which were deposited using e-beam evaporation. The device measurements were performed under Agilent 4516 in ambient conditions. The temperature-dependent transport measurements were performed using a cryogenic measurement setup. The temperatures of the devices were in the range of 77.4 to 300 K and were controlled by liquid nitrogen and a temperature controller (LakeShore 321 autotuning temperature controller).

As a comparison, some devices were annealed after metal electrode deposition to modify the contact between metal electrodes and MoS_2. The annealing was conducted at 200 °C for 2 h in a mixture of Ar and H_2 with flow rates of 200 and 20 sccm and a pressure of 1 Torr.[18,21]

Sensing Experiments. The fabricated devices were first wire-bonded to a chip carrier, which was then monitored onto a sealed sensing chamber. Electrical feedthrough and gas inlet and outlet were installed in the chamber. The sensing experiments were performed in Ar-diluted NO_2 or NH_3 at room temperature. The concentrations of each gas were adjusted by the flow rates of gases which were controlled by mass flow controllers. Both as-fabricated and annealed devices were tested under the same sensing setup and gas flow conditions.

Conflict of Interest: The authors declare no competing financial interest.

Acknowledgment. This work was supported by the Office of Naval Research and the Defence Threat Reduction Agency (DTRA). We acknowledge Professor Stephen Cronin of University of Southern California for access to the Raman facility.

Supporting Information Available: Additional optical microscopic images, Raman characterization, and device characteristics. This material is available free of charge *via* the Internet at http://pubs.acs.org.

REFERENCES AND NOTES

1. Yamazoe, N. Toward Innovations of Gas Sensor Technology. *Sens. Actuators, B* **2005**, *108*, 2–14.
2. http://www.epa.gov/Air/Nitrogenoxides/.
3. Kong, J.; Franklin, N. R.; Zhou, C. W.; Chapline, M. G.; Peng, S.; Cho, K. J.; Dai, H. J. Nanotube Molecular Wires as Chemical Sensors. *Science* **2000**, *287*, 622–625.
4. Snow, E. S.; Perkins, F. K.; Robinson, J. A. Chemical Vapor Detection Using Single-Walled Carbon Nanotubes. *Chem. Soc. Rev.* **2006**, *35*, 790–798.
5. Pengfei, Q. F.; Vermesh, O.; Grecu, M.; Javey, A.; Wang, O.; Dai, H. J.; Peng, S.; Cho, K. J. Toward Large Arrays of Multiplex Functionalized Carbon Nanotube Sensors for Highly Sensitive and Selective Molecular Detection. *Nano Lett.* **2003**, *3*, 347–351.
6. Gao, X. P. A.; Zheng, G. F.; Lieber, C. M. Subthreshold Regime Has the Optimal Sensitivity for Nanowire FET Biosensors. *Nano Lett.* **2010**, *10*, 547–552.
7. Hahm, J.; Lieber, C. M. Direct Ultrasensitive Electrical Detection of DNA and DNA Sequence Variations Using Nanowire Nanosensors. *Nano Lett.* **2004**, *4*, 51–54.
8. Cui, Y.; Wei, Q. Q.; Park, H. K.; Lieber, C. M. Nanowire Nanosensors for Highly Sensitive and Selective Detection of Biological and Chemical Species. *Science* **2001**, *293*, 1289–1292.
9. Zheng, G. F.; Patolsky, F.; Cui, Y.; Wang, W. U.; Lieber, C. M. Multiplexed Electrical Detection of Cancer Markers with Nanowire Sensor Arrays. *Nat. Biotechnol.* **2005**, *23*, 1294–1301.
10. Ganzhorn, M.; Vijayaraghavan, A.; Dehm, S.; Hennrich, F.; Green, A. A.; Fichtner, M.; Voigt, A.; Rapp, M.; von Lohneysen, H.; Hersam, M. C.; *et al.* Hydrogen Sensing with Diameter- and Chirality-Sorted Carbon Nanotubes. *ACS Nano* **2011**, *5*, 1670–1676.
11. Zhang, D. H.; Liu, Z. Q.; Li, C.; Tang, T.; Liu, X. L.; Han, S.; Lei, B.; Zhou, C. W. Detection of NO_2 down to ppb Levels Using Individual and Multiple In_2O_3 Nanowire Devices. *Nano Lett.* **2004**, *4*, 1919–1924.
12. Wei, T.-Y.; Yeh, P.-H.; Lu, S.-Y.; Wang, Z. L. Gigantic Enhancement in Sensitivity Using Schottky Contacted Nanowire Nanosensor. *J. Am. Chem. Soc.* **2009**, *131*, 17690–17695.
13. Yeh, P. H.; Li, Z.; Wang, Z. L. Schottky-Gated Probe-Free ZnO Nanowire Biosensor. *Adv. Mater.* **2009**, *21*, 4975–4978.
14. Kolmakov, A.; Klenov, D. O.; Lilach, Y.; Stemmer, S.; Moskovits, M. Enhanced Gas Sensing by Individual SnO_2 Nanowires and Nanobelts Functionalized with Pd Catalyst Particles. *Nano Lett.* **2005**, *5*, 667–673.
15. Zou, X. M.; Wang, J. L.; Liu, X. Q.; Wang, C. L.; Jiang, Y.; Wang, Y.; Xiao, X. H.; Ho, J. C.; Li, J. C.; Jiang, C. Z.; *et al.* Rational Design of Sub-Parts Per Million Specific Gas Sensors Array Based on Metal Nanoparticles Decorated Nanowire Enhancement-Mode Transistors. *Nano Lett.* **2013**, *13*, 3287–3292.
16. Schedin, F.; Geim, A. K.; Morozov, S. V.; Hill, E. W.; Blake, P.; Katsnelson, M. I.; Novoselov, K. S. Detection of Individual Gas Molecules Adsorbed on Graphene. *Nat. Mater.* **2007**, *6*, 652–655.
17. Wehling, T. O.; Novoselov, K. S.; Morozov, S. V.; Vdovin, E. E.; Katsnelson, M. I.; Geim, A. K.; Lichtenstein, A. I. Molecular Doping of Graphene. *Nano Lett.* **2008**, *8*, 173–177.
18. Radisavljevic, B.; Radenovic, A.; Brivio, J.; Giacometti, V.; Kis, A. Single-Layer Mos_2 Transistors. *Nat. Nanotechnol.* **2011**, *6*, 147–150.
19. Jariwala, D.; Sangwan, V. K.; Late, D. J.; Johns, J. E.; Dravid, V. P.; Marks, T. J.; Lauhon, L. J.; Hersam, M. C. Band-like Transport in High Mobility Unencapsulated Single-Layer MoS_2 Transistors. *Appl. Phys. Lett.* **2013**, *102*, 173107.
20. Jariwala, D.; Sangwan, V. K.; Wu, C. C.; Prabhumirashi, P. L.; Geier, M. L.; Marks, T. J.; Lauhon, L. J.; Hersam, M. C. Gate-Tunable Carbon Nanotube-MoS_2 Heterojunction p-n Diode. *Proc. Natl. Acad. Sci. U.S.A.* **2013**, *110*, 18076–18080.

21. Lopez-Sanchez, O.; Lembke, D.; Kayci, M.; Radenovic, A.; Kis, A. Ultrasensitive Photodetectors Based on Monolayer MoS_2. *Nat. Nanotechnol.* **2013**, *8*, 497–501.
22. Radisavljevic, B.; Kis, A. Mobility Engineering and a Metal-Insulator Transition in Monolayer MoS_2. *Nat. Mater.* **2013**, *12*, 815–820.
23. Sangwan, V. K.; Arnold, H. N.; Jariwala, D.; Marks, T. J.; Lauhon, L. J.; Hersam, M. C. Low-Frequency Electronic Noise in Single-Layer MoS_2 Transistors. *Nano Lett.* **2013**, *13*, 4351–4355.
24. Chuang, S.; Battaglia, C.; Azcatl, A.; McDonell, S.; Kang, J. S.; Yin, X.; Tosun, M.; Kapadia, R.; Fang, H.; Wallace, R. M.; *et al.* MoS_2 p-Type Transistors and Diodes Enabled by High Work Function MoO_x Contacts. *Nano Lett.* **2014**, *14*, 1337–1342.
25. Walia, S.; Balendhran, S.; Wang, Y. C.; Ab Kadir, R.; Zoolfakar, A. S.; Atkin, P.; Ou, J. Z.; Sriram, S.; Kalantar-zadeh, K.; Bhaskaran, M. Characterization of Metal Contacts for Two-Dimensional MoS_2 Nanoflakes. *Appl. Phys. Lett.* **2013**, *103*, 232105.
26. Late, D. J.; Liu, B.; Matte, H. S. S. R.; Dravid, V. P.; Rao, C. N. R. Hysteresis in Single-Layer MoS_2 Field Effect Transistors. *ACS Nano* **2012**, *6*, 5635–5641.
27. Das, S.; Chen, H. Y.; Penumatcha, A. V.; Appenzeller, J. High Performance Multilayer MoS_2 Transistors with Scandium Contacts. *Nano Lett.* **2013**, *13*, 100–105.
28. Popov, I.; Seifert, G.; Tomanek, D. Designing Electrical Contacts to MoS_2 Monolayers: A Computational Study. *Phys. Rev. Lett.* **2012**, *108*, 156802.
29. Lee, G. H.; Yu, Y. Y.; Cui, X.; Petrone, M.; Lee, C. H.; Choi, M. S.; Lee, D. Y.; Lee, C.; Yoo, W. J.; Watanabe, K.; *et al.* Flexible and Transparent MoS_2 Field-Effec Transistors on Hexagonal Boron Nitride−Graphene Heterostructures. *ACS Nano* **2013**, *7*, 7931–7936.
30. Liu, H.; Si, M.; Deng, Y.; Neal, A. T.; Du, Y.; Najmaei, S.; Ajayan, P. M.; Lou, J.; Ye, P. D. D. Switching Mechanism in Single-Layer Molybdenum Disulfide Transistors: An Insight into Current Flow across Schottky Barriers. *ACS Nano* **2014**, *8*, 1031–1038.
31. He, Q. Y.; Zeng, Z. Y.; Yin, Z. Y.; Li, H.; Wu, S. X.; Huang, X.; Zhang, H. Fabrication of Flexible MoS_2 Thin-Film Transistor Arrays for Practical Gas-Sensing Applications. *Small* **2012**, *8*, 2994–2999.
32. Li, H.; Yin, Z. Y.; He, Q. Y.; Li, H.; Huang, X.; Lu, G.; Fam, D. W. H.; Tok, A. I. Y.; Zhang, Q.; Zhang, H. Fabrication of Single- and Multilayer MoS_2 Film-Based Field-Effect Transistors for Sensing NO at Room Temperature. *Small* **2012**, *8*, 63–67.
33. Late, D. J.; Huang, Y. K.; Liu, B.; Acharya, J.; Shirodkar, S. N.; Luo, J. J.; Yan, A.; Charles, D.; Waghmare, U.; Dravid, V. P.; *et al.* Sensing Behavior of Atomically Thin-Layered MoS_2 Transistors. *ACS Nano* **2013**, *7*, 4879–4891.
34. Perkins, F. K.; Friedman, A. L.; Cobas, E.; Campbell, P. M.; Jernigan, G. G.; Jonker, B. T. Chemical Vapor Sensing with Monolayer MoS_2. *Nano Lett.* **2013**, *13*, 668–673.
35. Sarkar, D.; Liu, W.; Xie, X.; Anselmo, A. C.; Mitragotri, S.; Banerjee, K. MoS_2 Field-Effect Transistor for Next-Generation Label-Free Biosensors. *ACS Nano* **2014**, 10.1021/nn5009148.
36. Castellanos-Gomez, A.; Poot, M.; Steele, G. A.; van der Zant, H. S. J.; Agrait, N.; Rubio-Bollinger, G. Elastic Properties of Freely Suspended MoS_2 Nanosheets. *Adv. Mater.* **2012**, *24*, 772–775.
37. Lee, Y. H.; Zhang, X. Q.; Zhang, W. J.; Chang, M. T.; Lin, C. T.; Chang, K. D.; Yu, Y. C.; Wang, J. T. W.; Chang, C. S.; Li, L. J.; *et al.* Synthesis of Large-Area MoS_2 Atomic Layers with Chemical Vapor Deposition. *Adv. Mater.* **2012**, *24*, 2320–2325.
38. Lee, Y. H.; Yu, L. L.; Wang, H.; Fang, W. J.; Ling, X.; Shi, Y. M.; Lin, C. T.; Huang, J. K.; Chang, M. T.; Chang, C. S.; *et al.* Synthesis and Transfer of Single-Layer Transition Metal Disulfides on Diverse Surfaces. *Nano Lett.* **2013**, *13*, 1852–1857.
39. Liu, K. K.; Zhang, W. J.; Lee, Y. H.; Lin, Y. C.; Chang, M. T.; Su, C.; Chang, C. S.; Li, H.; Shi, Y. M.; Zhang, H.; *et al.* Growth of Large-Area and Highly Crystalline MoS_2 Thin Layers on Insulating Substrates. *Nano Lett.* **2012**, *12*, 1538–1544.
40. Shi, Y. M.; Zhou, W.; Lu, A. Y.; Fang, W. J.; Lee, Y. H.; Hsu, A. L.; Kim, S. M.; Kim, K. K.; Yang, H. Y.; Li, L. J.; *et al.* van der Waals Epitaxy of MoS_2 Layers Using Graphene as Growth Templates. *Nano Lett.* **2012**, *12*, 2784–2791.
41. Najmaei, S.; Liu, Z.; Zhou, W.; Zou, X. L.; Shi, G.; Lei, S. D.; Yakobson, B. I.; Idrobo, J. C.; Ajayan, P. M.; Lou, J. Vapour Phase Growth and Grain Boundary Structure of Molybdenum Disulphide Atomic Layers. *Nat. Mater.* **2013**, *12*, 754–759.
42. van der Zande, A. M.; Huang, P. Y.; Chenet, D. A.; Berkelbach, T. C.; You, Y. M.; Lee, G. H.; Heinz, T. F.; Reichman, D. R.; Muller, D. A.; Hone, J. C. Grains and Grain Boundaries in Highly Crystalline Monolayer Molybdenum Disulphide. *Nat. Mater.* **2013**, *12*, 554–561.
43. Zhan, Y. J.; Liu, Z.; Najmaei, S.; Ajayan, P. M.; Lou, J. Large-Area Vapor-Phase Growth and Characterization of MoS_2 Atomic Layers on a SiO_2 Substrate. *Small* **2012**, *8*, 966–971.
44. Yu, Y. F.; Li, C.; Liu, Y.; Su, L. Q.; Zhang, Y.; Cao, L. Y. Controlled Scalable Synthesis of Uniform, High-Quality Monolayer and Few-Layer MoS_2 Films. *Sci. Rep.* **2013**, *3*, 1866.
45. Lin, Y. C.; Zhang, W. J.; Huang, J. K.; Liu, K. K.; Lee, Y. H.; Liang, C. T.; Chu, C. W.; Li, L. J. Wafer-Scale MoS_2 Thin Layers Prepared by MoO_3 Sulfurization. *Nanoscale* **2012**, *4*, 6637–6641.
46. Wang, H. T.; Lu, Z. Y.; Xu, S. C.; Kong, D. S.; Cha, J. J.; Zheng, G. Y.; Hsu, P. C.; Yan, K.; Bradshaw, D.; Prinz, F. B.; *et al.* Electrochemical Tuning of Vertically Aligned MoS_2 Nanofilms and Its Application in Improving Hydrogen Evolution Reaction. *Proc. Natl. Acad. Sci. U.S.A.* **2013**, *110*, 19701–19706.
47. Kong, D. S.; Wang, H. T.; Cha, J. J.; Pasta, M.; Koski, K. J.; Yao, J.; Cui, Y. Synthesis of MoS_2 and $MoSe_2$ Films with Vertically Aligned Layers. *Nano Lett.* **2013**, *13*, 1341–1347.
48. Ji, Q. Q.; Zhang, Y. F.; Gao, T.; Zhang, Y.; Ma, D. L.; Liu, M. X.; Chen, Y. B.; Qiao, X. F.; Tan, P. H.; Kan, M.; *et al.* Epitaxial Monolayer MoS_2 on Mica with Novel Photoluminescence. *Nano Lett.* **2013**, *13*, 3870–3877.
49. Wu, S. F.; Huang, C. M.; Aivazian, G.; Ross, J. S.; Cobden, D. H.; Xu, X. D. Vapor-Solid Growth of High Optical Quality MoS_2 Monolayers with Near-Unity Valley Polarization. *ACS Nano* **2013**, *7*, 2768–2772.
50. Ling, X.; Lee, Y. H.; Lin, Y. X.; Fang, W. J.; Yu, L. L.; Dresselhaus, M.; Kong, J. Role of the Seeding Promoter in MoS_2 Growth by Chemical Vapor Deposition. *Nano Lett.* **2014**, *14*, 464–472.
51. Mak, K. F.; Lee, C.; Hone, J.; Shan, J.; Heinz, T. F. Atomically Thin MoS_2: A New Direct-Gap Semiconductor. *Phys. Rev. Lett.* **2010**, *105*, 136805.
52. Splendiani, A.; Sun, L.; Zhang, Y. B.; Li, T. S.; Kim, J.; Chim, C. Y.; Galli, G.; Wang, F. Emerging Photoluminescence in Monolayer MoS_2. *Nano Lett.* **2010**, *10*, 1271–1275.
53. Wang, X. S.; Feng, H. B.; Wu, Y. M.; Jiao, L. Y. Controlled Synthesis of Highly Crystalline MoS_2 Flakes by Chemical Vapor Deposition. *J. Am. Chem. Soc.* **2013**, *135*, 5304–5307.
54. Chen, J. R.; Odenthal, P. M.; Swartz, A. G.; Floyd, G. C.; Wen, H.; Luo, K. Y.; Kawakami, R. K. Control of Schottky Barriers in Single Layer MoS_2 Transistors with Ferromagnetic Contacts. *Nano Lett.* **2013**, *13*, 3106–3110.
55. Qiu, H.; Pan, L. J.; Yao, Z. N.; Li, J. J.; Shi, Y.; Wang, X. R. Electrical Characterization of Back-Gated Bi-layer MoS_2 Field-Effect Transistors and the Effect of Ambient on Their Performances. *Appl. Phys. Lett.* **2012**, *100*, 123104.
56. Ou, J. Z.; Carnpbell, J. L.; Yao, D.; Wlodarski, W.; Kalantar-zadeh, K. *In Situ* Raman Spectroscopy of H_2 Gas Interaction with Layered MoO_3. *J. Phys. Chem. C* **2011**, *115*, 10757–10763.
57. Balendhran, S.; Deng, J. K.; Ou, J. Z.; Walia, S.; Scott, J.; Tang, J. S.; Wang, K. L.; Field, M. R.; Russo, S.; Zhuiykov, S.; *et al.* Enhanced Charge Carrier Mobility in Two-Dimensional High Dielectric Molybdenum Oxide. *Adv. Mater.* **2013**, *25*, 109–114.
58. Wang, Y. C.; Ou, J. Z.; Balendhran, S.; Chrimes, A. F.; Mortazavi, M.; Yao, D. D.; Field, M. R.; Latham, K.; Bansal, V.; Friend, J. R.; *et al.* Electrochemical Control of Photoluminescence in Two-Dimensional MoS_2 Nanoflakes. *ACS Nano* **2013**, *7*, 10083–10093.

59. Sze, S. M.; Ng, K. K. *Physics of Semiconductor Devices*, 3rd ed.; John Wiley & Sons, Inc.: New York, 2007.
60. Lee, K.; Gatensby, R.; McEvoy, N.; Hallam, T.; Duesberg, G. S. High Performance Sensors Based on Molybdenum Disulfide Thin Films. *Adv. Mater.* **2013**, *25*, 6699–6702.
61. Javey, A.; Kong, J. *Carbon Nanotube Electronics*; Springer Science+Business Media: New York, 2008.
62. Abbas, A.; Liu, G.; Liu, B. L.; Zhang, L.; Liu, H.; Ohlberg, D.; Wu, W.; Zhou, C. W. Patterning, Characterization and Chemical Sensing Applications of Graphene Nanoribbon Arrays down to 5 nm Using Helium Ion Beam Lithography. *ACS Nano* **2014**, *8*, 1538–1546.
63. Gong, C.; Zhang, H. J.; Wang, W. H.; Colombo, L.; Wallace, R. M.; Cho, K. J. Band Alignment of Two-Dimensional Transition Metal Dichalcogenides: Application in Tunnel Field Effect Transistors. *Appl. Phys. Lett.* **2013**, *103*, 053513.
64. Fontana, M.; Deppe, T.; Boyd, A. K.; Rinzan, M.; Liu, A. Y.; Paranjape, M.; Barbara, P. Electron–Hole Transport and Photovoltaic Effect in Gated MoS_2 Schottky Junctions. *Sci. Rep.* **2013**, *3*, 1634.
65. Nah, J.; Kumar, S. B.; Fang, H.; Chen, Y. Z.; Plis, E.; Chueh, Y. L.; Krishna, S.; Guo, J.; Javey, A. Quantum Size Effects on the Chemical Sensing Performance of Two-Dimensional Semiconductors. *J. Phys. Chem. C* **2012**, *116*, 9750–9754.
66. Cui, X. D.; Freitag, M.; Martel, R.; Brus, L.; Avouris, P. Controlling Energy-Level Alignments at Carbon Nanotube/Au Contacts. *Nano Lett.* **2003**, *3*, 783–787.
67. Gui, E. L.; Li, L. J.; Zhang, K. K.; Xu, Y. P.; Dong, X. C.; Ho, X. N.; Lee, P. S.; Kasim, J.; Shen, Z. X.; Rogers, J. A.; *et al.* DNA Sensing by Field-Effect Transistors Based on Networks of Carbon Nanotubes. *J. Am. Chem. Soc.* **2007**, *129*, 14427–14432.